191
2/1/80

H. 625

LBL-8413
UC- 32

Lawrence Berkeley Laboratory
UNIVERSITY OF CALIFORNIA

IMAGE PROCESSING OF SMALL PROTEIN-CRYSTALS
IN ELECTRON MICROSCOPY

David Alan Feinberg

MASTER

November 1978

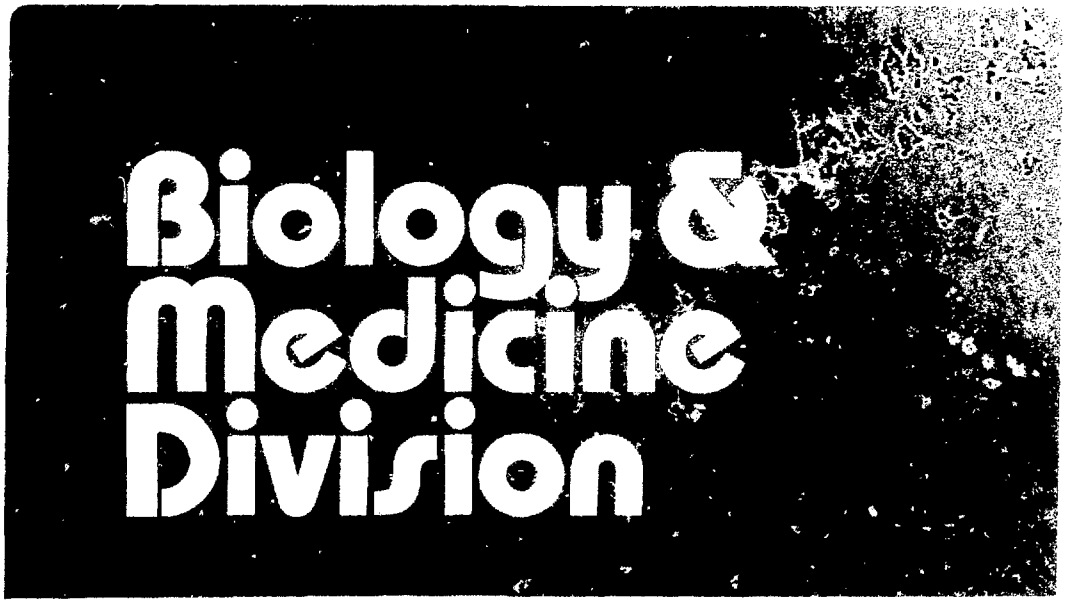

Prepared for the U.S. Department of Energy under Contract W-7405-ENG-48

IMAGE PROCESSING OF SMALL PROTEIN-CRYSTALS IN ELECTRON MICROSCOPY

David Alan Feinberg

Lawrence Berkeley Laboratory
University of California
Berkeley, CA 94720

ABSTRACT

This electron microscope study was undertaken to determine whether high resolution reconstructed images could be obtained from statistically noisy micrographs by the super-position of several small areas of images of well-ordered crystals of biological macromolecules. Methods of rotational and translational alignment which use Fourier space data were demonstrated to be superior to methods which use Real space image data. After alignment, the addition of the diffraction patterns of four small areas did not produce higher resolution because of unexpected image distortion effects. A method was developed to determine the location of the distortion origin and the coefficients of spiral distortion and pincushion/barrel distortion in order to make future correction of distortions in electron microscope images of large area crystals.

TABLE OF CONTENTS

INTRODUCTION

A. Background: Spatial Averaging of Low-Dose Images of Protein Crystal Gives High Resolution Structure

Improvement in the electron microscope resolution of biological structure has been achieved by reducing radiation damage to the specimen. Specimen damage due to inelastic scattering of electrons is minimized by making low electron dose exposures of specimens in highly ordered two-dimensional crystals and then carrying out a spatial average over the resulting statistically noisy images. (see Kuo (1) and Glaeser (2)).

Low-dose exposure techniques have produced high resolution 2-dimensional projected structures of several biological protein including: purple membrane of Halobacterium halobium to 6.6Å resolution, (3) catalase protein to 9Å,(4) and of T4 bacteriophage gene product 32* I.

The statistically noisy low-dose images of all the above specimens were spatially averaged, or Fourier filtered to exhibit their well defined average protein structure. Spatial averaging has been done most successfully with computerized Fourier transforms. However, laser optical techniques on optical diffractometers are also commonly used in several laboratories. The electron diffraction patterns of the crystalline specimens are noise filtered by setting all spots not on the reciprocal lattice to zero. Calculating the inverse-Fourier transform of this masked diffraction pattern gives the well-defined, average specimen structure.

B. Problems Which Limit the Success of Spatial Averaging

Several properties are required of the specimen for spatial averaging to be successful. The protein molecules must be arranged in a highly ordered 2-dimensional periodic lattice (crystal) to obtain electron diffraction patterns. This crystal must have a large surface area so that many unit cells are spatially averaged to show the highest resolution protein structure in the image.

Some specimens form small but well ordered crystals, which have too small an area for spatial averaging to show welldefined structure, e.g., gap junction and acetyl choline receptor protein. The small size of these crystals is assumed to be the limiting factor in obtaining higher resolution. This limitation may be overcome either by improved techniques of specimen purification and crystalization, or by the computer image processing techniques which are to be discussed in this paper.

Another problem encountered in high resolution electron microscopy is that distortions in the image limit the specimen area usable for spatial averaging. In the outer regions of the image, distortions cause changes in unit cell magnification and orientation. The computed diffraction patterns of distorted specimen regions have destructive interference of high resolution coefficients, and thus high resolution diffraction pattern spots are absent in the patterns. For example, the image of Gp32* I protein, used as data in the following work, has a 3.76 percent difference in magnification between the center and perimeter regions of the image plate and a difference in unit cell orientation of 1.13 degrees, due to pincushion/barrel

distortion and spiral distortion. Some suggestions for correcting these distortions are discussed later in this work.

C. Purpose: Attempts to Combine Several Areas of Low-Dose Imaged Specimen to Develop and Implement in a Spatial Averaging Technique; and a Method of Correcting Distortions

To overcome the limitation in spatial averaging of specimens in small sized, well-ordered crystals (patches), the diffraction patterns of several patches could be combined. Before coherent addition of the computed diffraction patterns is possible, the lattice vectors of the patches must be aligned. In this work, different methods of rotational and translational alignment are compared with respect to cost, accuracy, and the ease of including them in a dynamic image alignment and addition computer program.

In order to correct for the pincushion and spiral distortions in the test specimen image, a method is developed to find the distortion origin in the image and the distortion coefficients. The distortion origin and coefficients could then be used in a bilinear interpolation of the digitized image to remove the distortions.

D. A Brief Summary of the Results

For both the rotational and translational alignment of the small areas, the methods working with diffraction patterns in Fourier space were found to be superior to methods directly using digitized images in real space. After the alignment of four small image areas of Gp32* I protein, the combination of all their data did not show

higher resolution in the final diffraction pattern. The presence of distortions in the test specimen image prevented the coherent addition of diffraction spots.

A mathematical expression for distorted unit cell lattice vectors was derived for the first time and could be used to solve for the unknown position of distortion origin. The bilinear interpolation which used the distortion origin and coefficients found in this work, did not correct for distortion in the test specimen image.

II. DATA: A LOW-DOSE IMAGE OF T4 BACTERIOPHAGE GENE PRODUCT 32*I (DNA HELIX-DESTABILIZING PROTEIN), AND A HIGH-DOSE IMAGE OF SPIRILLUM SERPENS CELL WALL PROTEIN

To simulate the problems involved in aligning patches of protein crystal from separate images, small areas of a large crystal in a single crystal were digitized with different relative angles and lateral displacements between them. Their unknown relative angles are chosen not to exceed 4^{o} because prealignment within this angle on a laser optical bench is possible before scanning.

The high-dose image of cell wall protein (6) was used only for the initial testing of the rotational alignment algorithms. The high-dose image gave a diffraction pattern with strong intensity in low resolution spots which were good for testing cross-correlation algorithms. However, due to the high level of radiation damage in these high electron dose images, the attainable resolution is already reached in the diffraction patterns of the seperate specimen areas, and combining several of these areas will not show higher resolution in spatial averaging. For this reason, a low-dose image of Gp32*I protein was used in alignment experiments and the experiment to combine diffraction patterns. The low-dose image areas have a much lower signal-to-noise ratio than the high-dose images and a decrease in the accuracy of the alignment of the Spirillum serpens is expected.

Both the Spirillum serpens cell wall protein image and the Gp32*I image were made by Dr. Wah Chiu (5,6). The cell wall protein was negatively stained and imaged with a high electron dose of approximately 100 electrons/A^{2} and at 40,000X magnification. The

unstained Gp32*I protein was glucose embedded and imaged with a low electron dose of approximately 3 electrons/Å^2 and at 40,000X magnification.

The Gp32*I crystal is of orthorhombic space group with 2-dimensional lattice vector constants measured to be a = 629Å and b = 47.3Å.

A resolution of 3.7Å has been measured in electron diffraction patterns of large crystal areas of Gp32*I, indicating that the specimen used for data in the following experiments is well ordered.

The images are digitized for computer processing on a Perkin-Elmer scanning densitometer. A scanning step size of 10μm is used to scan the 6mm by 6mm areas of specimen to produce 600 by 600 square arrays of image intensities. The 10μm step represents a 2.5Å step at the specimen is used, which is considered ideal for retrieval of Fourier coefficients of the structure out to approximately 7Å resolution.

To include more unit cells in spatial averaging without having to use a larger Fast Fourier Transforms, the 600 by 600 array is 2-by-2 averaged to make a 300 by 300 array. From this 300 by 300 array is taken a 200 by 200 array, and this 4mm by 4mm digitized image area is used as data for all subsequent work. The 2-by-2 averaging of optical densities limits the attainable resolution in there image areas to approximately 14Å instead of the 7Å before averaging.

III. TRANSLATIONAL ALIGNMENT

A. Translational Alignment Using a Cross-Correlation in Real Space

Two protein crystals are laterally aligned when their unit cells have the same crystallographic origin. By displacing the crystals to the same origin, structurally similar points can be superimposed. The maximum displacement between two crystals' origin is the length of the unit cell due to the periodicity in the crystal.

When two crystals are laterally aligned, the cross-correlation function (CCF) of the two crystals shows a peak or maximum value. The general form of the CCF of any two data sets, t and h, is the correlation integral;

$$CCF(d) = \int_{-\infty}^{\infty} t(x) \cdot h(x+d)\, dx \qquad (1)$$

The value of the CCF, when evaluated at several different displacements, will be maximized when t and h are best aligned. Defining t and h to be the 200 by 200 arrays of image intensities and rewritting equation (1) in discrete form gives;

$$CCF(d_x,d_y) = \sum_{y=1}^{200} \sum_{x=1}^{200} t(x,y) \cdot h(x+d_x,y+d_y) \qquad (2)$$

where x,y are the indexes of array elements in columns and rows respectively, and

d_x, d_y are the displacements between the two arrays, in columns and rows respectively.

The maximum displacement to be used in the CCF is readily calculated from the unit cell dimension. This displacement is the number of rows and columns by which image h can be displaced without repeating the evaluation of the CCF at an identical crystallographic position, due to the specimen's periodic nature. The image area covered by one unit cell, divided by the scan step size of each array element, (pixel size), gives the maximum d_x and d_y at which the CCF is to be evaluated:

$$\text{maximum displacement} = \frac{\text{unit cell length x magnification in image}}{\text{pixel size}}$$

$$d_{x\ \text{maximum}} = \frac{62.9\text{Å} \times 40{,}000}{20 \times 10^4 \text{Å}}$$

$$= 12.58$$

$$d_{y\ \text{maximum}} = \frac{47.3\text{Å} \times 40{,}000}{20 \times 10^4 \text{Å}}$$

$$= 9.46$$

The values calculated above are correct if the unit cells' lattice vectors are parallel to the sampling grid of the scan. The image of Gp32* I protein crystal was scanned at a 40^o angle relative to the lattice vectors, therefore d_x maximum = 24 and d_y maximum = 12 are used. The CCF is evaluated at integer row and column displacements and the total number of evaluations is 24 x 12 = 288 displacement positions.

B. Translational Alignment By Shifting the Phases of Diffraction Spots in Fourier Space

The crystallographic origin of the specimen may be displaced in real space, as described above, or equivalently changed in Fourier space by a particular change of the Fourier transform. It is shown below that a displacement in real space, $\vec{d}$, is equivalent to changing the phase of the Fourier transform by $2\pi\vec{S}\cdot\vec{d}$. Using this property of the Fourier transform, two protein crystals are translationally aligned by shifting the phases of their diffraction patterns. The displacement that gives the best alignment is determined by minimizing the phase discrepancies in a least squared error minimization program.

The relationship between a real space displacement and a change in the Fourier transform is seen in the Fourier transform of function $\phi(\vec{r})$:

$$\Phi(s) = \int_{-\infty}^{\infty} \phi(\vec{r}) \cdot e^{-i2\pi\vec{s}\cdot\vec{r}} dr \qquad (3)$$

where

$\phi(\vec{r})$ = real space function (the image)

$\vec{r}$ = spatial vector

$\vec{s}$ = spatial frequency vector

$\Phi(\vec{s})$ = Fourier transform of $\phi(\vec{r})$

A spatial displacement of $\phi(\vec{r})$ to $\phi(\vec{r} + \vec{d})$ correspondingly changes the Fourier transform to $\Phi_d(\vec{s})$ where;

$$\Phi_d(\vec{s}) = \int_{-\infty}^{\infty} \phi(r + d) \cdot e^{-i2\pi\vec{s}\cdot\vec{r}} \cdot dr$$

$$= \Phi(\vec{s}) \cdot e^{i2\pi\vec{s} \cdot \vec{d}} \qquad (4)$$

Using the complex function form of $\Phi(\vec{s})$, allows for the defining of phase and amplitude.

$$\Phi(\vec{s}) = R(\vec{s}) + iI(\vec{s}) \qquad (5)$$

where R(s) = real component of $\Phi(\vec{s})$

$I(\vec{s})$ - imaginary component of $\Phi(\vec{s})$

and $\Phi(\vec{s}) = A(\vec{s}) \cdot e^{i\theta(\vec{s})}$ (6)

where $A(\vec{s})$ = Fourier Amplitude

$$= |\Phi(\vec{s})|$$

$$= \sqrt{R(\vec{s})^2 + I(\vec{s})^2}$$

$\theta(\vec{s})$ = Phase

$$= \arctan\ I(\vec{s})/R(\vec{s})$$

Finally, rewriting $\Phi_d(\vec{s})$ in terms of phase and amplitude shows that a real space translation by $\vec{d}$ is equivalent to shifting the phases by $+2\pi\vec{s}\ \vec{d}$;

$$\Phi_d(\vec{s}) = A\ (\vec{s})\ .\ e^{i\theta(\vec{s})}\quad e^{i2\pi\vec{s}\cdot\vec{d}} \tag{7}$$

$$= A\ (\vec{s})\ \cdot\ e^{i(\theta(\vec{s})\ +\ 2\pi\vec{s}\ \cdot\ \vec{d}}$$

Two Gp32* I crystals are translationally aligned to one another by changing the phases of one of their computed diffraction patterns until they best match the phases of the other diffraction pattern in a least square fit. Only the phases of the reciprocal lattice reflections are used in the least squares function $F(\vec{d})$ which is minimized:

$$F(d) = \sum_{i=1}^{n} \theta_{1_i} - (\theta_{2_i} + 2\pi\vec{s}_i \cdot \vec{d})^2 \tag{8}$$

θ_{1i} = phase of i diffraction spot in pattern 1,

θ_{2i} = phase at identical diffraction spot i in pattern 2,

$\vec{s}_i$ = spatial frequency vector at diffraction spot i,

$\vec{d}$ = real space displacement vector (μm)
$(d_{row}\ 20\mu m + d_{column}\ .20\mu m)$,

n = total number of diffraction spots.

Diffraction patterns of two 4mm square image areas of Gp32* I protein are used for data in the above least squares function. The two image areas are rotationally aligned but have an unknown displacement between the crystalographic origin of their unit cells. Six reciprocal lattic reflections, see Figure 1, are used in equation (8) with the following Miller indeces:

$$(h,k) = (2,1);\ (2,0);\ (2,\bar{1});\ (3,1);\ (3,\bar{1});\ (4,0).$$

C. Results: Phase Shifting Method Worked Best

By fitting the phases of the two crystals' diffraction patterns, a relative displacement between their crystallographic origins is found; y displacement = 10.95Å (.5475 rows), and x-displacement = 11.4Å (.57 columns). Using these values of d_x, d_y, gives an average difference between phases of the identical diffraction spots equal to 20.6 degrees. The phases of the diffraction spots are shown in Table 1. both before and after changing the phase with the above displacements. In each 5 by 5 array, the center element (3,3) is at the indicated row, column position in the 200 by 200 diffraction patterns and corresponds to the reciprocal lattic reflection of (h, k) value shown.

The real space cross-correlation method did not show a peak value at any displacement position. The Cross-correlation function fluctuated around a value of 4.6030×10^{-10} at all displacement positions. A position at which the two images are superimposed was not found with this method.

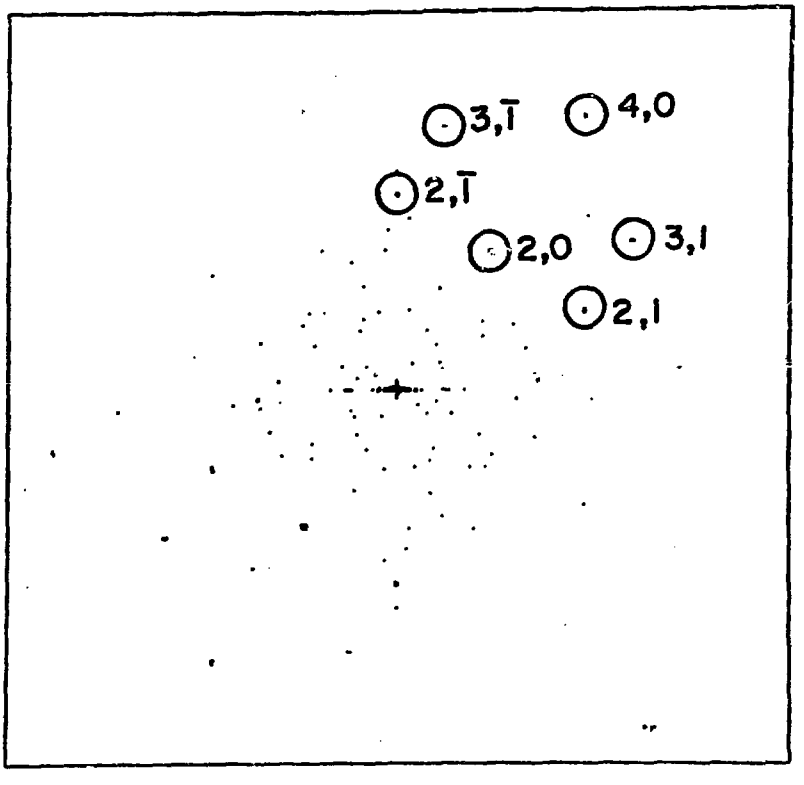

XBL798-3733

Figure 1. Calculated Diffraction Pattern of T4 Bacteriophage Gene Product 32 I. The circled diffraction spots are used in several of the cross-correlation experiments.

Table 1. The phases of selected reflections of two diffraction patterns of Gp32*I protein are shown before and after the phase shifting of Pattern 2 to match the phases of reflections in Pattern 1. The reflections are located here in the center array element with the indicated row and column locations in the 200 by 200 diffraction patterns.

Pattern 1					Pattern 2 (before phase shifting)					Pattern 2 (after phase shifting)				
					ROW = 67	COL = 104	H = 2	K = -1						
170	31	130	-161	81	23	101	-32	-7	-100	148	-94	172	-124	-177
-84	76	-108	-69	81	76	123	94	-122	-161	-118	-32	-22	162	163
120	-34	0	-38	32	-22	-90	0	57	-159	-175	156	23	22	-155
-39	-116	-22	86	-59	158	13	-130	175	-2	46	-60	-163	-179	44
-128	119	-124	103	-55	62	-179	-90	-91	27	-9	149	-82	-43	114
					ROW = 78	COL = 119	H = 2	K = 0						
-88	129	-104	96	-64	-112	81	33	148	-25	-18	-145	-154	0	-133
136	125	-92	90	65	-44	-146	69	-131	15	91	28	-77	122	-52
-87	125	-110	-63	117	77	116	112	-91	-119	-107	-29	0	-156	-145
-57	180	-178	150	-152	11	19	-96	97	-177	-132	-84	-160	73	-162
-109	-52	63	44	48	1	-48	107	5	-125	-101	-110	84	21	-59
					ROW = 90	COL = 134	H = 2	K = 1						
55	-162	-132	105	2	137	67	-88	155	99	-120	-151	93	16	-0
66	-127	-61	46	117	51	-29	-142	137	168	-165	154	81	39	109
155	-71	150	22	-155	117	13	-178	78	-35	-58	-122	90	21	-53
-88	-122	88	31	-146	3	-171	48	90	-129	-131	94	-7	74	-106
2	168	-56	-111	-82	-73	-174	-28	117	5	-166	132	-42	142	69
					ROW = 79	COL = 143	H = 3	K = 1						
28	-11	130	27	170	48	-98	171	-139	-44	87	-20	-71	18	152
162	-86	-157	170	-30	-177	-130	62	-18	-51	-98	-11	-134	-180	-174
-143	97	169	171	114	-95	-138	-38	-17	94	26	22	167	-138	12
-176	122	166	26	-8	7	-130	134	-17	-114	169	71	15	-97	-154
128	135	78	34	81	164	-16	39	114	60	7	-134	-40	75	60
					ROW = 55	COL = 113	H = 3	K = -1						
-118	-163	-32	16	97	-86	92	27	-110	-34	-65	152	127	30	145
66	141	-81	50	-149	-91	-21	171	133	-159	-29	80	-48	-46	61
-112	129	102	-144	-158	-180	125	-80	54	-50	-76	-92	102	-85	-149
-132	-84	54	-38	43	1	-14	46	-132	112	145	169	-91	130	54
-21	-31	74	-66	100	120	-80	10	-166	82	-54	145	-86	138	65

A cost comparison of the two methods shows that the real space method is approximately 3 times the cost of the method of shifting the phases in Fourier space. The phase shifting method cost approximately $1.10 when using six diffraction spots.

The difference in cost is due to the greater number of multiplications in evaluating the real space CCF at each new displacement (4000 multiplications) than is needed in the phase shifting method (approximately 300 multiplications). It should be noted that the cost of the two Fast Fourier transforms ($1.60) for the phase shifting method, is not included in this cost comparison because these transforms must be calculated eventually to combine diffraction patterns in the procedure, to be discussed in Chapter VI.

IV. ROTATIONAL ALIGNMENT

A. Orientation of Specimen is Measured from Diffraction Pattern Intensities

The two procedures of rotational alignment to be discussed in this chapter require information on the orientation the reciprocal lattice vectors of diffraction patterns. There are two reasons for using diffraction patterns for rotational alignment. The first reason is that the researcher may use a laser optical bench to see the diffraction pattern's power spectrum (Fourier amplitude squared, $A(\vec{s})^2$) and determine the orientation of the specimen crystal to within a few degrees error. This angle is used for initial alignment of the image on the scanning densitometer and to prealign images before computer processing. This prealignment reduces the size of the angle in which a computer algorithm must search for a position of rotational alignment.

A second reason for working in Fourier space is to accomplish rotational alignment independent of lateral displacements between the two images. If one works in Fourier space, only the amplitude of diffraction spots are needed for seeing the orientation of lattice vectors, and not the phases.

B. Rotating the Image in Real Space and Evaluating a Cross-Correlation Function in Fourier Space

The rotational cross-correlation function is evaluated at different angles by an iteration of the following procedures. First,

one of two digitized images is rotated by an angular displacement using a bilinear interpolation algorithm, to be described below. Second, a Fast Fourier Transform is computed to give the diffraction pattern of the rotated image and a stationary image's diffraction pattern is also computed. Third, identical diffraction spots in the above two patterns are used to evaluate the rotational cross-correlation function, both weighted and non-weighted. By evaluating the rotational CCF at several new angles, a cross-correlation peak will show the angle of best alignment. These procedures of rotation, Fourier transform, masking, and calculating the CCFs, are shown in the flowchart in Figure 2.

To rotate a digitized image requires a method of determining new optical densities at points located between the measured densities on the original scanning grid. These new densities at non-integer rows and column positions are determined with the bilinear interpolation algorithm, (see Grano (8)). The new densities are calculated from the four adjacent originally scanned optical densities, using the equation shown in Figure 3. The 200 by 200 array which represents the rotated image area, is interpolated from a slightly larger image area, a 220 by 220 array, to prevent the corners of the rotated area from moving off of the original scanned image area, (see Figure 4).

The rotated image area in the 200 by 200 array is Fast Fourier transformed to give a rotated diffraction pattern. The diffraction spots of this rotated pattern are angularly displaced by the same angle of image rotation, $\Delta\theta$, into new array locations. These diffraction spots are usually split among two or three array elements.

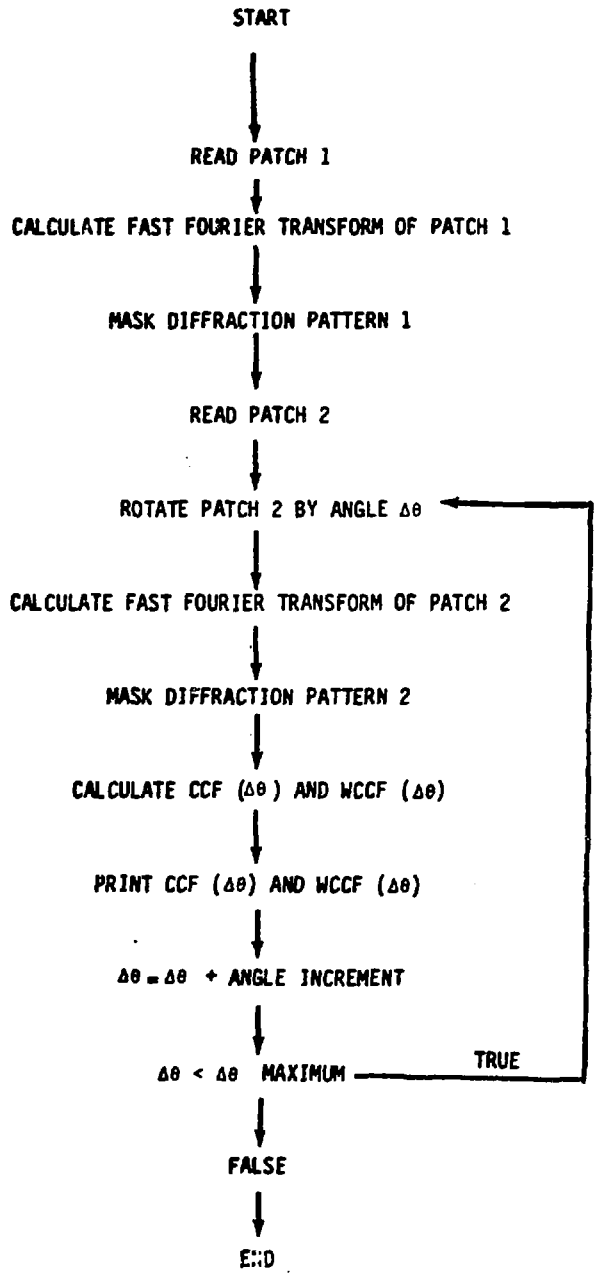

Figure 2. Flowchart of Real Space method of Rotational Alignment. The image data is rotated using the bilinear interpolation algorithm and the least-squares difference functions, weighted and non-weighted (WCCF and CCF), are calculated.

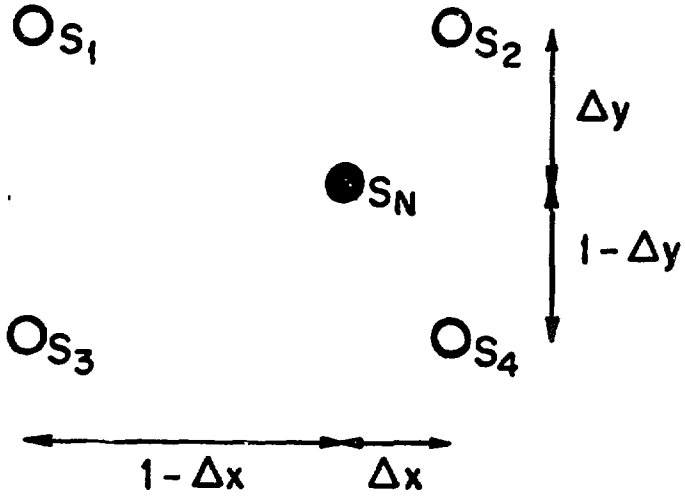

$$S_N = (1-\Delta x)\cdot((1-\Delta y)\cdot S_2 + (\Delta y)\cdot S_4) + (\Delta x)\cdot((1-\Delta y)\cdot S_1 + (\Delta y)\cdot S_3))$$

S_N - value of spot at new location

S_1, S_2, S_3, S_4 - values of 4 regularly spaced adjacent array elements

$\Delta y, \Delta x$ - distance between S_N and S_2 in units of array fraction

XBL798-3734

Figure 3. Bilinear Interpolation Scheme. The equation shows how the new density, S_n, is calculated from the four adjacent scanned optical densities.

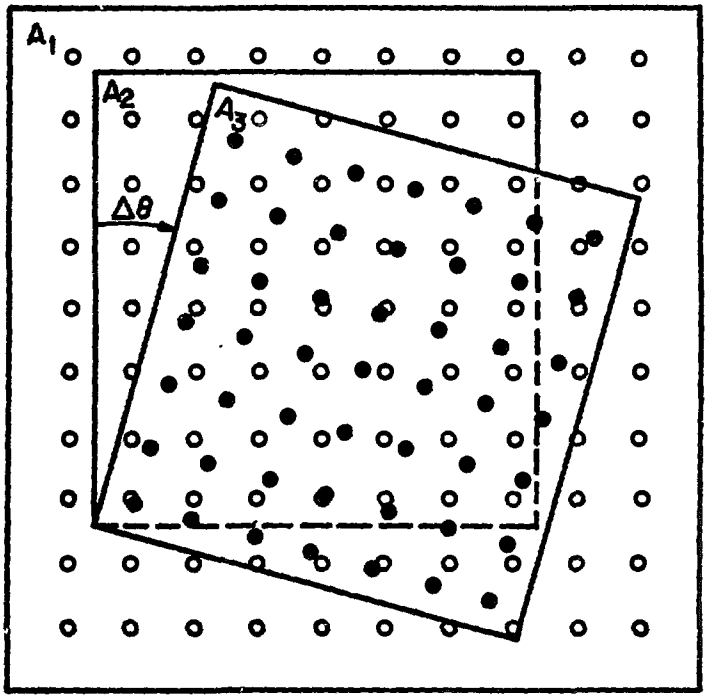

o – Light dots are image optical densities found with scanning densitometer along regular spaced gria

● – Dark dots are densities of image area rotated by angle $\Delta\theta$ using bilinear interpolation

A_1 – Array of originally scanned optical densities of image

A_2 – Image data array taken from A_1

A_3 – Array of rotated image data

XBL798-3737

Figure 4. Illustration of how an array of optical densities, A_1, is rotated by an Angle, $\Delta\theta$, to give an array of rotated image data, A_2.

Consequently, for different $\Delta\theta$ displacements, only small relative changes among the two or three intensities of the split diffraction spot are usually observed.

A masking procedure is employed to include all the split diffraction spots in the calculation of the rotational CCF of two diffraction patterns, yet exclude most of the surrounding spots which are due to statistical noise in the image. In this procedure, all Fourier intensities are set to zero, except for the several 3 by 3 array element areas in which the diffraction spots are located. The positions of these 3 by 3 subarrays are centered on the diffraction spots of the stationary image and at identical row and column coordinates in the rotated image's diffracton pattern. If the angle $\Delta\theta$ is too great then the diffraction spots may be rotated to array elements outside of these specified 3 by 3 subarrays and in effect these specified subarrays are analogous to windows through which the rotated diffraction pattern is observed. When the diffraction pattern is rotated to the same orientation as the stationary images' diffraction pattern, their identical diffraction spots will be located in the same array elements and the rotational CCF will show a peak value.

The summed least squares difference of the two masked diffraction patterns is calculated at various angles of rotation to find the best angle of alignment. In equation 9 below, the magnitude of the cross-term $|A_{1_{jk}} \cdot A_{2_{ijk}}(\Delta\theta)|$, is exactly equivalent to the cross-correlation function of the two patterns which shows a positive peak when the patterns are aligned. This least square function shows a negative peak or minimum value at the position of the cross-correlation peak due to the negative sign of this cross-term.

$$F(\Delta\theta) = \sum_{k=1}^{N} \sum_{j=1}^{3} \sum_{i=1}^{3} \left(A_{1_{ijk}} - A_{2_{ijk}}(\Delta\theta) \right)^2 \qquad (9)$$

$A_{1_{ijk}}$ - 3 by 3 array around diffraction spot k in the stationary pattern 1.

$A_{2_{ijk}}$ - same 3 by 3 array in $\Delta\theta$ rotated diffraction pattern 2.

$\Delta\theta$ = angle of rotation

N = total number of diffraction spots.

In equation 10, the squared difference of diffraction spots is weighted by the distance between the spot and the diffraction pattern center:

$$F_w(\Delta\theta) = \sum_{k=1}^{N} \sum_{j=1}^{3} \sum_{i=1}^{3} W_K \cdot \left(A_{1_{ijk}} - A_{2_{ijk}}(\Delta\theta) \right)^2 \qquad (10)$$

where $W_k = \sqrt{(x - 101)^2 + (y - 101)^2}$

is the weight used in the least squares fit given to the diffraction spot which is at array index (x,y) = (row,column) and the center of the computer diffraction pattern = (101,101). This gives greater weight in the least squares fit to the higher frequency diffraction spots, which more accurately show angular displacements between the two patterns. For example, in the diffraction pattern of Gp32* I which is centered at row and column coordinates = (101,101) in the

200 by 200 array, a 1.0^{0} rotation of the pattern displaces the high spatial frequency spot, 4,0 by 1.9 rows and 1.1 columns. The low spatial frequency spot h,k = $(\bar{1},0)$ is displaced .2 rows and .5 columns.

The above weighted and non weighted least squares functions are evaluated at ten different angular displacements between the two image areas. One of the images is rotated by several different angles and the functions are evaluated at each new angle using six diffraction spots: (h,k) = $(2,\bar{1})$, (2,0), (2,1), (3,1), $(3,\bar{1})$, (4,0).

C. Evaluating the Angular Cross-Correlation Function Entirely in Fourier Space Without Rotating the Image in Real Space

The following method is used to evaluate the angular CCF totally in Fourier space, which thus eliminates the interaction of two procedures; rotating the image with the bilinear interpolation and calculating the Fast Fourier Transform. Such a method was first proposed and used by Frank and Saxton (9,10) to align non-periodic identical biological particles in statistically noisy images. Fourier intensities are bilinearly interpolated along annuli at a common radius in the power specta of the two images, and these intensities are used to calculate an angular cross-correlation of the two images.

In the work presented here, intensities are bilinearly interpolated along arcs subtending diffraction spots in the two diffraction patterns, and are used to calculate the angular CCF. The arcs from one diffraction pattern are stored in one dimensional arrays and a rotation of the pattern is mapped into a displacement, or reindexing, of the arcs. A rotational CCF of two diffraction patterns is

evaluated at several different angular displacements by iteratively reindexing the arrays of intensities of one diffraction pattern and multiplying these intensities with the intensities at the same array index from the second stationary diffraction pattern. The value of the Rotational CCF (RCCF) at a particular angle of rotation is equal to the summed product of the two sets of arcs;

$$RCCF(d) = \sum_{k=1}^{n} \sum_{i=1}^{m} Arc1_{k,i} \cdot Arc2_{k,i+d}$$

$Arc1_{k,i}$ = intensity(i) on arc through diffraction spot k in the pattern 1.

$Arc2_{k,i+d}$ = intensity (i+d) on arc through diffraction spot k in pattern 2.

d = increment of array displacement which is equivalent to an angular displacement

m = total number of intensities in arcs.

n = total number of diffraction spots used in the function.

The arcs are, in effect, unfolded into linear arrays, and an angular rotation is changed into a reindexing of the arcs from one of the two patterns. The sampling increment along the arc is readily determined

by the radial distance (R) from the center of the pattern to the diffraction spot, the arc length ($\Delta\theta$) in radians and the number of array elements, N:

$$\text{sampling increment} = \frac{R \cdot \Delta\theta}{N}$$

Three or more arcs can be passed through diffraction spots to better locate spots which are split over several array elements. Intensities are interpolated along three arcs passing through a diffraction spot at slightly different radii from the diffraction pattern center to make three dimensional arrays. The 3-dimensional arrays from two diffraction patterns are multiplied and summed in the same way as the one-dimensional arcs so that all of the data is used in calculating the CCF. Figure (5) shows how Fourier intensities are found along three arcs through a diffraction spot.

For both the one-arc CCF and three-arc CCF, the following reciprocal lattice reflections are used:

$$(h,k) = (2,\bar{1}),\ (2,0),\ (2,1),\ (3,1),\ (3,\bar{1}),\ (4,0)$$

In the three-arc CCF the two additional arcs are found at $\pm.3$ array element radial distance from the arcs used in the one-arc CCF. The number of intensities sampled on the arcs, 100, is twice the number of array elements, N, used in the CCF, 50, so that the displacement by reindexing does not exceed the arc length.

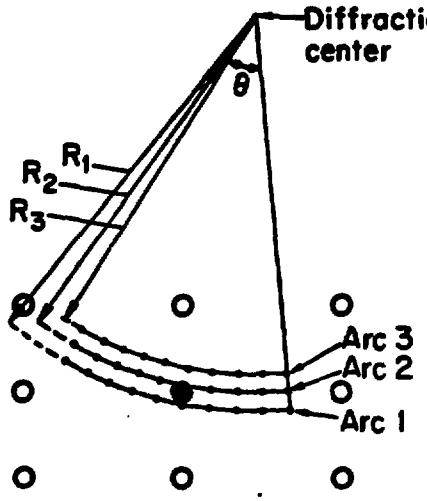

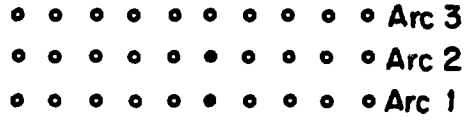

Arcs stored in 3-D array

O – Calculated diffraction pattern amplitudes in 200 by 200 array

o – Amplitudes found with bilinear interpolation along arcs and stored in a 3-dimensional array which is used in the 3-arc rotational cross-correlation

XBL798-3732

Figure 5. Illustration of bilinear interpolation of intensities along arcs at different radii through a diffraction spot.

D. Results: Relative Expense of The Arc Method in Fourier Space and the Rotation Method in Real Space

The graphs in Figure 6 and 7 display the results of the rotational alignment experiments. The method of rotating images in real space gave the same minimum at .017 radians in the least squares function, see Figure 6, for both the weighted function and the non-weighted function. The Fourier space arc method showed cross-correlation peaks at .0185 radians for the one-dimensional array arcs and at .0214 radians for the three-dimensional array arcs. The positions of the maxima and minima represent the best angles of alignment of the two images.

The difference in these angles is very small compared to the accuracy required to coherently add the fourth order diffraction spot $(h,k) = 4.0)$ from several different diffraction patterns. There is a .0015 radians (.000026 degrees) difference between the real space rotation method and the single-arc method (one-dimensional array CCF). This angular difference results in an error of displacement between unit cells of which is much less than the 14Å attainable resolution in the image.

The different peak position in the 3-arc method may be explained by more statistical noise included in the three interpolated arcs than in one-arc passing through the center of the diffraction spot. Two of the three arcs subtend regions in which the diffraction spot may not be located, thus more noise is included in the data.

The fact that the weighted function in the real space rotation method did not give a different peak position than the non-weighted

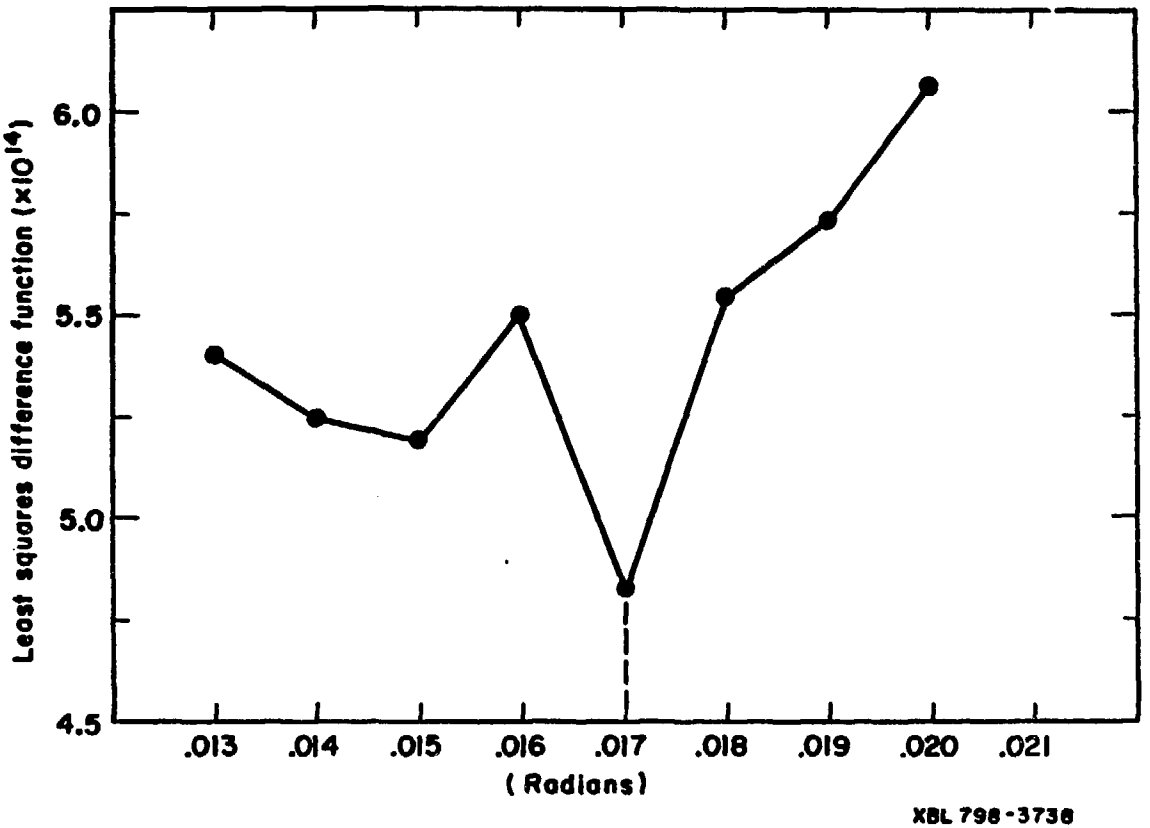

Figure 6(a) Graph shows the results of Real space rotational alignment method.

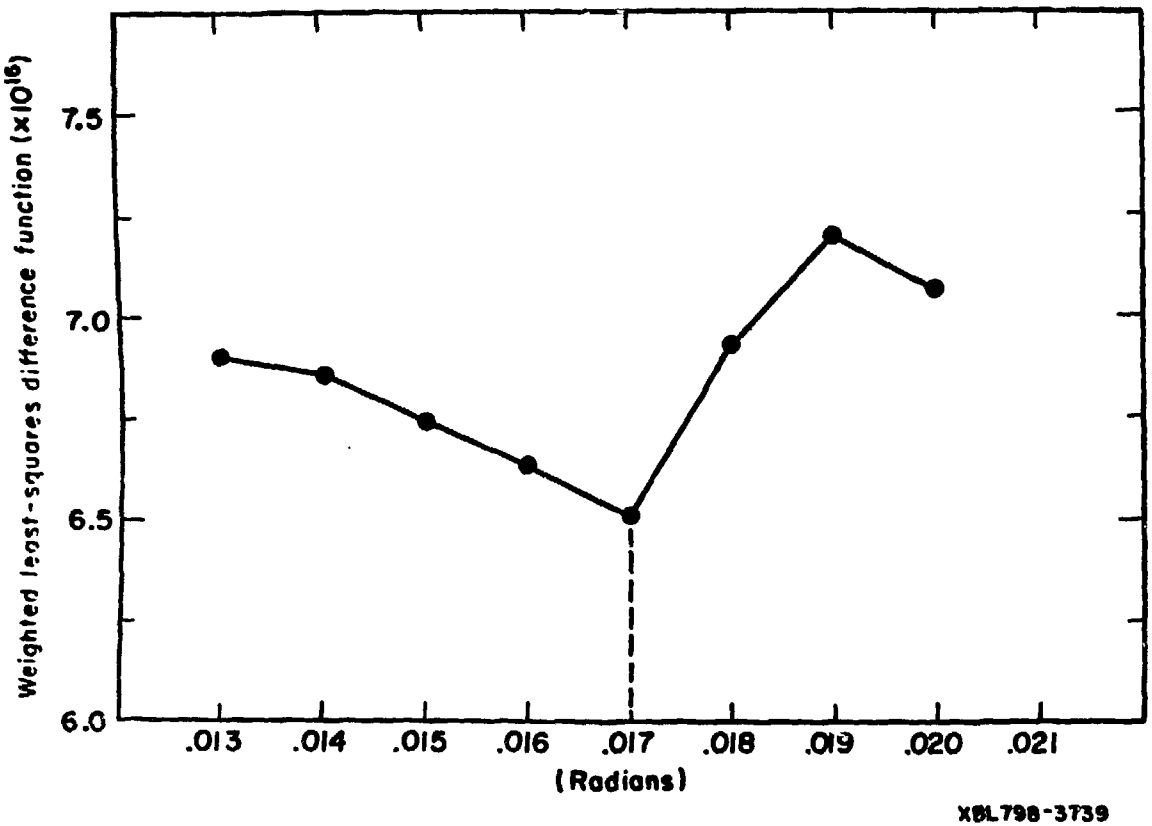

Figure 6(b) Graph shows the results of Real space rotational alignment method using the weighted least-squares difference function.

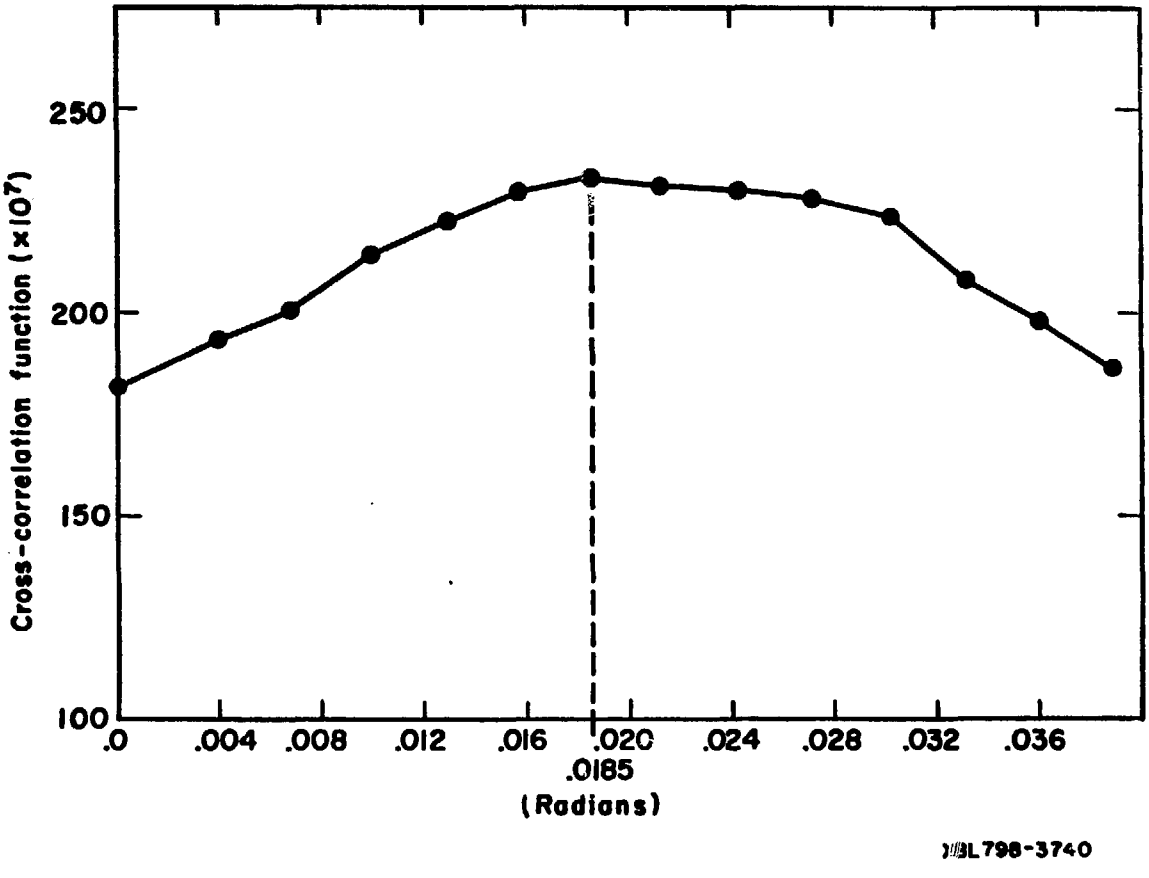

Figure 7(a) 1-arc Cross-correlation function results.

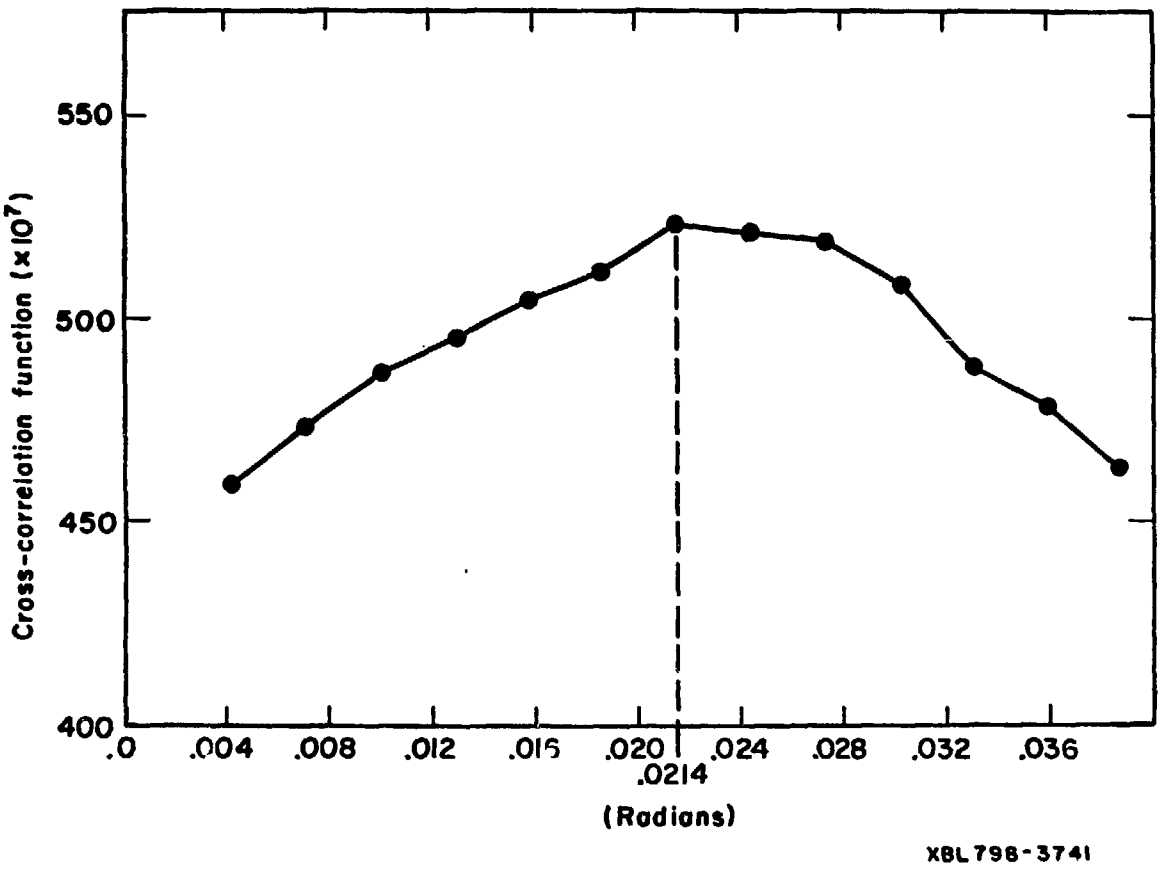

Figure 7(b) 3-arc Cross-correlation function results.

function may be explained by the large number of low frequency diffraction spots used in the fit. The predominent number of spots at lesser radii in sum have much greater contribution to the value of the minimization function than the more heavily weighted (4,0) spot. A different weighting function may still improve the accuracy of the fit, perhaps one which is proportional to a higher power of the radius (e.g., $radius^2$).

The cost of computation time to rotationally align the two patchs using the arc method was $2.00, about one fourth the cost of the real space rotation method (at $7.80). The difference in cost is due to the fact that much less computation time is required for the two fast fourier transforms and bilinear interpolation of arcs of 100 array elements than is required for the real space rotation method, which required seven image rotations and eight Fast Fourier transforms. The cost of rotational alignment may become an important consideration when several patchs are aligned and super-imposed.

V. COMBINATION OF DIFFRACTION PATTERNS OF FOUR IMAGE AREAS

A. Diffraction Patterns are Combined to Give Higher Resolution in Spatial Averaging.

Combining several diffraction patterns of aligned image areas increases the number of unit cells to be spatially averaged, and the combined data should therefore show higher resolution diffraction spots. The separate specimen patchs have too few unit cells for spatial averaging and therefore the maximum attainable resolution of the image is not reached. The Fourier coefficients of several aligned patchs will add with constructive interference and increase the signal-to-noise ratio of the diffraction spots. It is necessary for the identical diffraction spots of the several diffraction patterns to have the same phases and position in Fourier space for their constructive-interference to occur. The increased signal-to-noise ratio of the diffraction spot makes the spot more discernable above the average noise level in Fourier space. This better defines these spots that are already observable in the separate diffraction patterns and shows new diffraction spots which are not observed before combining the patterns. The appearance of new diffraction spots in the combined diffraction pattern is directly due to an increased number of unit cells used in spatial averaging and results in a better defined reconstructed image.

B. The ADDAR Computer Program Translationally Aligns and Adds Together Several Diffraction Patterns

Diffraction patterns of image areas at the same orientation angle are used for data in a program which shifts the phases of the patterns for translational alignment and adds the identical Fourier coefficients

from the two patterns to make a combined pattern. The Combined pattern which results from adding two or more diffraction patterns is used for fitting the phases of the next pattern to be added to the Combined pattern. The method of phase shifting has been described in section III.B. The Fourier coefficients in the 200 by 200 arrays are combined by the addition of complex numbers. Figure 8 shows a flow chart of the ADDAR program's procedure of combining any number of diffraction patterns.

Four diffraction patterns of different image areas are combined into one pattern using the ADDAR program. These image areas were rotationally aligned by the method described in section IV, using the following displacement angles in radians: (0.0), (-0.0055), (0.017), (0.014). These diffraction patterns of rotationally aligned image areas were stored on magnetic tape and could be read into the ADDAR program in any sequence to see if using any one particular diffraction pattern first gives a different final Combined Pattern.

C. Results: Resolution in Combined Pattern

The results of the addition experiment are shown in the table of Table 2, where the reciprocal lattice reflections from a single diffraction pattern are compared to the final Combined Pattern. The amplitudes of these reflections show a definite change in signal-to-noise ratio between the diffraction spots located in the center of each 5 by 5 array and the surrounding noise spots.

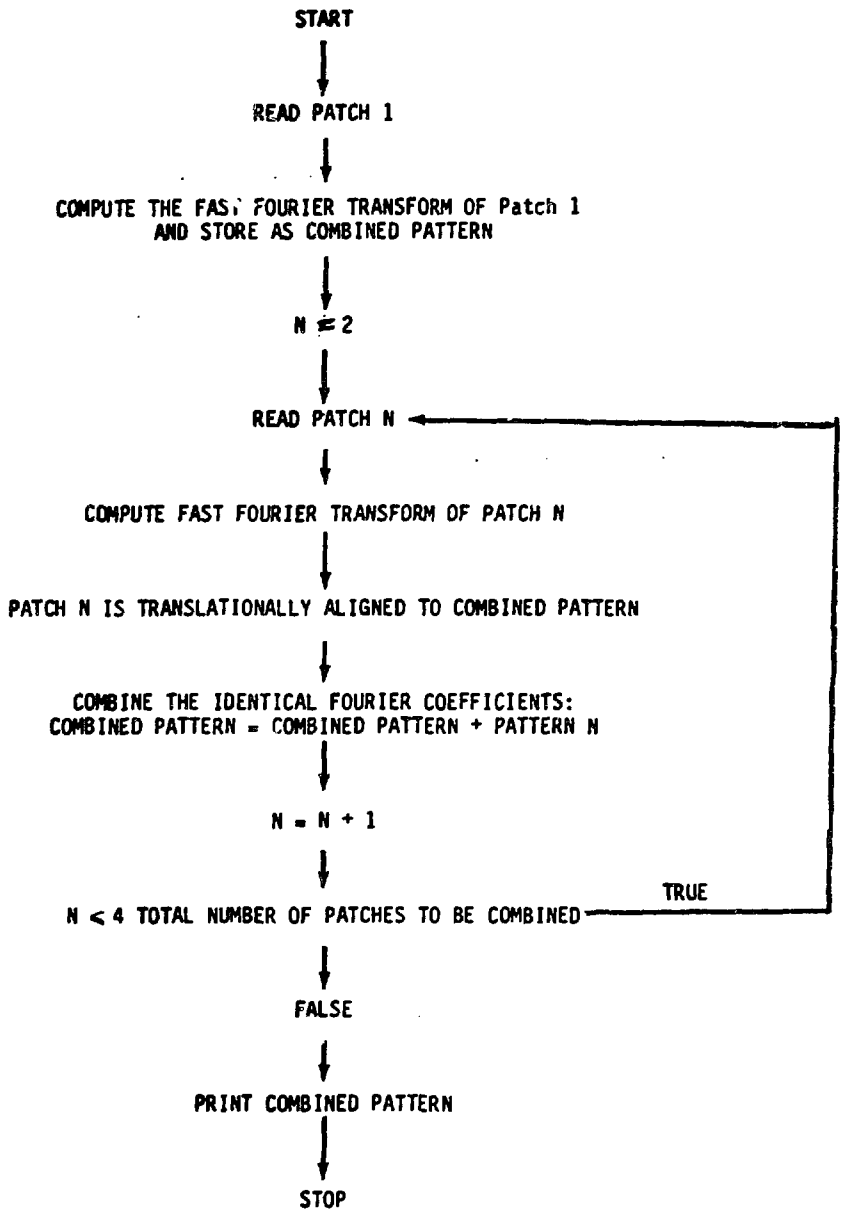

Figure 8. Flowchart of ADDAR Computer Program which adds Fourier coefficients from aligned diffraction patterns.

Table 2. Fourier Amplitudes in the region of six diffraction spots in circles from one of the four diffraction patterns (separate pattern) to be combined and from the diffraction pattern made from combining the four patterns (combined pattern).

SEPARATE PATTERN					COMBINED PATTERN				
H,K = 2,I					ROW, COLUMN = 67,104				
912	596	1733	514	1321	1207	162	3303	4161	1370
1295	292	1080	1035	1985	2571	1868	4358	4401	3641
1621	2914	5561	2383	694	7519	2591	(16065)	4191	3648
1465	2102	2367	704	1348	4378	5219	6302	4455	1347
182	1822	988	2223	341	2932	1952	2486	4468	5816
H,K = 2.0					ROW, COLUMN = 78,119				
532	1302	981	1088	2429	1012	303[illegible]	5229	3175	2661
855	797	956	462	746	1201	18[illegible]	2216	1901	3080
1152	1460	3879	1752	1845	6200	5[illegible]6	(16877)	6181	1885
924	894	1012	779	1419	1958	4417	4858	3454	2060
628	467	1548	610	2094	2150	2672	2462	479	985
H,K = 2,1					ROW, COLUMN = 90,134				
233	944	1707	639	1399	2074	1269	3619	944	1044
677	735	292	2129	631	1645	843	787	2195	1486
549	1632	3854	2553	968	2795	6548	(11084)	4258	697
1285	1348	1332	450	645	2455	3517	3856	1010	3219
705	1747	265	1538	1221	2771	2983	358	3193	1911
H,K = 3,1					ROW, COLUMN = 79,143				
946	509	871	436	627	2418	689	1972	2344	317
684	1995	1138	2097	901	2259	1232	7192	1168	1111
1153	576	1723	1168	123	1219	8076	(13395)	4489	1371
1515	512	1908	884	2427	2818	3786	2979	1359	3277
1113	1093	1650	722	516	2239	974	2126	2036	2196
H,K = 3,1					ROW, COLUMN = 59,113				
880	694	647	750	1061	3064	2781	2121	4084	4219
2381	2987	695	1533	708	2753	2186	4558	3893	2479
1528	2341	1852	1105	1380	3476	2453	(11902)	6657	652
2062	1908	750	2207	1013	1957	2873	7107	2676	2121
1138	2846	478	924	1377	3391	5658	1259	2437	2423

Table 2. Cont'd

SEPARATE PATTERN H,K = 4,0					COMBINED PATTERN ROW, COLUMN = 56,137				
553	1701	951	1872	1613	2378	639	3260	2769	579
1088	2232	639	1805	1127	485	2783	1178	3350	3219
569	5927	1944	2095	1638	2089	5217	17910	3251	2555
1985	5430	3928	1503	1145	8289	11028	21649	7781	677
1017	2023	1168	328	903	3260	2295	5766	6101	3110

The expected appearance of new diffraction spots in the Combined pattern, which were not seen in the seperate patterns, did not occur. Reciprocal lattice vectors were used to determine the position of these diffraction spots and no new amplitude peaks were discernable above the noise level in the Combined pattern. Thus the Fourier coefficients of these reflections did not combine constructivly to rise above the surrounding noise.

To be certain that the total number of unit cells in the combined pattern was sufficient to show the expected spots at new reciprocal lattice locations, a comparison was made to a diffraction pattern of a single crystal area which has 3 times the size of one patch. The diffraction pattern of the larger crystal showed numerous diffraction spots, which are not seen in the Combined Pattern. In this large crystal, the number of spatially averaged unit cells is 3/4 the total number in the combined pattern. Based on this comparison, the addition of more diffraction patterns of small patches to the Combined pattern would not show new spots.

Possible reasons for the non-coherent addition of diffraction patterns were investigated. The algorithms used in the ADDAR program were checked for program errors. To test the Phase shifting algorithm, an image area was displaced by bilinear interpolation to a new origin: 2.5 row and 1. column displacement. The diffraction pattern of this displaced image was then laterally aligned by the phase shifting algorithm to the diffraction pattern of the original undisplaced image area, resulting in an auto-correlation of the image area. The algorithm found a displacement of 2.51 row and 1.1 columns, resulting

in a .5Å error of unit cell position which would not cause destructive interference of coefficients at the missing reflections.

Checking the data used in the addition experiment revealed that the diffraction patterns of areas of the crystal in the perimeter regions of the image had their identical diffraction spots located at slightly different positions. This discovery of the presence of distortions in the image led the author into the distortion correction work which is discussed in the remaining sections of this paper.

VI. DISTORTION CORRECTION

A. Resolution in Spatial Averaging as Limited by Distortions

Distortions in the images of periodic specimens reduce the number of unit cells usable in spatial averaging. The presence of pincushion/barrel and spiral distortions in images causes a change in the length and orientation of unit cells in the perimeter region of the image. These changes in unit cell dimensions prevent constructive interference of high spatial frequency coeffieients. If the number of unit cells in the central undistorted region of the image is too few, then these high resolution diffraction spots will not be seen. In the case of a non-periodic specimen, distortions reduce the accuracy in measuring specimen lengths but do not reduce the resolution obtained in the image.

The general mathematical description of pincushion distortion and spiral distortion in an image, (Hillier (11), Liebman (12)), is as follows;

$$\vec{r}' = \vec{r} + \psi|\vec{r}|^3\hat{r} + \theta\cdot|\vec{r}|^3\cdot(\hat{k}\times\hat{r}) \qquad (13)$$

$\vec{r}$ = vector from distortion origin to the position of the specimen in the image, in the absence of distortion.

$\vec{r}'$ = distorted vector

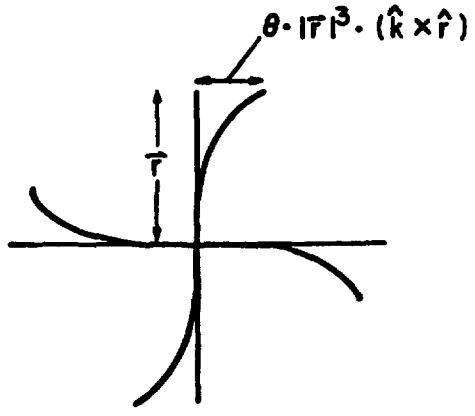

a) Spiral distortion

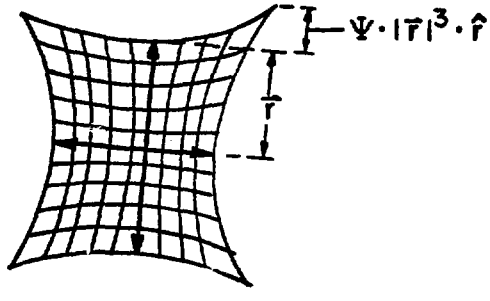

b) Pincushion distortion

XBL798-3736

Figure 9. Illustration of distortion effects on a regularly spaced grid.

Ψ = pincushion distortion coefficient

θ = spiral distortion coefficient

$\hat{k}$ = unit vector orthonormal to image plane

$\hat{r}$ = unit vector in direction of $\vec{r}$.

B. Presence of Distortions in the Test Image of Gp32*-I Protein

Both pincushion and spiral distortions were observed in the image of Gp32*I by changes in location of reciprocal lattice reflection positions in diffraction patterns from different regions of the image. A comparison of diffraction patterns of 2mm squared areas from the perimeter of the image and the center of the image showed different orientation and length of reciprocal lattice vectors. The reflections in the diffraction pattern of the perimeter image region compared to the pattern of the central region are 3.76 percent closer to the center of the pattern and are rotated by 1.1313^{o}. The decrease in radial positions of reflection represents a 3.76 percent increase in image magnification, and this change is attributed to pincushion distortion. The rotation of the unit cell vectors and reciprocal lattice vectors is caused by spiral distortions as shown in equation (13) above and to a lesser extent caused by the pincushion distortion as will be shown in Section VI.C.

Correction of distortions in an image by an interpolation method requires the accurate determination of the center of distortion in the image. Due to the $\vec{r}^3$ dependence in eqation (13) an error in locating the distortion origin greatly reduces the accuracy of determining the effect of distortions in different areas of the image. The origin of distortions will be different in each image due to small differences in the loaded position of the photographic plate in the electron microscope. In the next 2 sections, a method is developed and used to find the origin of distortions and distortion coefficients (Ψ,θ) in the Gp32*I image which was used as data for the experiments on alignment and addition of specimen areas.

C. Derivation of Distorted Specimen Lattice Vectors

The expression for the distorted unit cell vectors are first derived here in terms of the non-distorted vector $\vec{r}$ to the image point. However, $\vec{r}$ cannot be measured on the distorted image where only the distorted vector $\vec{r}'$ can be measured. By inverting equation (13), the $\vec{r}$ is expressed in terms of $\vec{r}'$ and $\vec{r}_o$, a displacement vector from the arbitrarily chosen coordinate origin to the true origin of distortions. The final expression at the end of this section has only 3 unknowns, ($\vec{r}_o$,θ and Ψ), and describes the effects of the distortions on the unit cell lattice vectors in all regions of the image. The three unknown parameters can be solved for using measurements of distorted lattice vectors in three or more regions of the image.

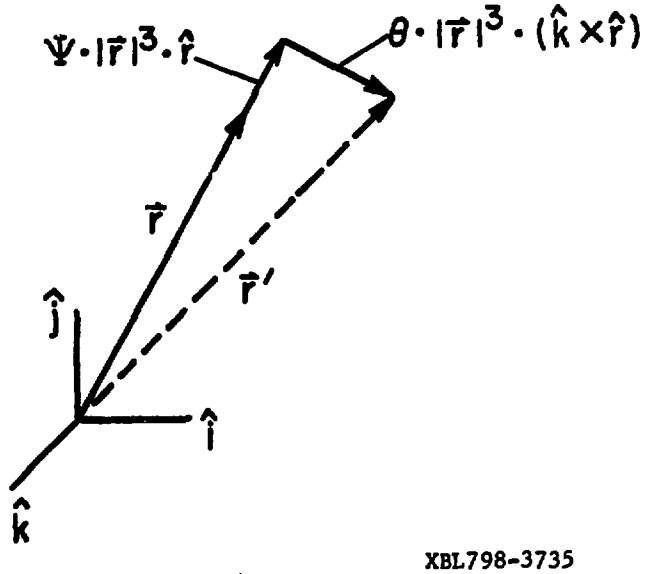

XBL798-3735

Figure 10. Diagram shows a vector $\vec{r}$ in the image plane, $(\hat{i}, \hat{j})$, distorted by pincushion and spiral distortions into the vector $\vec{r}'$.

In the following equations, all primed vectors are distorted quantities of the corresponding unprimed vectors. Therefore the distorted vector from the distortion origin to a point in the distorted image is written as before;

$$\vec{r}' = \vec{r} + \psi|\vec{r}|^3\vec{r} + \theta|\vec{r}|^3(\quad \times \hat{r}) \tag{14}$$

where

$\vec{r}$ = vector from distortion origin to specimen's position without distortion.

$\vec{r}'$ = distorted vector r from distortion origin to specimen's position.

θ = pincushion distortion coefficient

ψ = spiral distortion coefficient

$\hat{r}$ = unit vector in r direction

$\hat{k}$ = unit vector orthonormal to plane of image plate

Any vector lying in the image plane, or more specifically the distorted unit cell vector $\vec{b}'$, can be expressed as the difference between two measurable vectors from the distortion origin;

$$b' = \vec{r}'_2 - \vec{r}'_1 \tag{15}$$

The $\vec{r}'_2$ vector may be written as a distortion function, F, of undistorted vector r_1 and b:

$$\vec{r}'_2 = \vec{r}'_1 + \vec{b}' \tag{16}$$

$$= F\,(\vec{r}_1 + \vec{b})$$

and

$$\vec{r}'_1 = F\,(\vec{r}_1)$$

$$= \vec{r}_1 + \psi|\vec{r}_1|^3 \cdot \hat{r} + \theta|r_1|^3(\hat{k} \times \hat{r}). \tag{17}$$

Knowing that the crystal lattice vector is much smaller than the r_1 vector, the Taylor Expansion of the function follows:

$$\vec{r}'_2 = F(\vec{r}_1 + \vec{b})$$

$$= F(\vec{r}_1) + (\vec{b}\cdot\bar{\nabla})F(\vec{r}_1) + 1/2\ (\vec{b}\cdot\bar{\nabla})\ (\vec{b}\cdot\bar{\nabla})\ F(\vec{r}_1)$$

$$+ \ldots. + \frac{1}{n}\ (\vec{b}\cdot\bar{\nabla})^n F(\vec{r}_1) \tag{18}$$

where

$$(\vec{b}\cdot\bar{\nabla})\,\vec{r} = \left(b_x \frac{\partial}{\partial x} + b_y \frac{\partial}{\partial y}\right)(x\hat{i} + y\hat{\partial})$$

$$= b$$

and

$$(\vec{b}\cdot\bar{\nabla})\vec{r}^2 = (\vec{b}\cdot\bar{\nabla})\,(x^2 + y^2)$$

$$= 2\,\vec{b}\cdot\vec{r}$$

Dropping the third and higher order terms in equation (18) and substituting equation (17) for $F(\vec{r}_1)$ gives;

$$\vec{r}'_2 = F(\vec{r}_1) + \vec{b}\cdot\bar{\nabla}\left(\vec{r}_1 + \psi|\vec{r}_1|^3\cdot\vec{r} + \theta|r_1|^3\cdot(\hat{k}\times\hat{r})\right)$$

$$= F(\vec{r}_1) + \vec{b}\,(1 + \psi|\vec{r}_1|^2) + 2\,\psi\vec{r}_1(\vec{b}\cdot\vec{r}_1) \qquad (19)$$

$$+ 2\theta\cdot(\vec{r}_1\cdot\vec{b})\cdot(\vec{k}\times\vec{r}_1) + \theta\cdot|\vec{r}_1|^2\cdot(\vec{k}\times\vec{r})$$

By substituting the above equation (19) for $\vec{r}'_2$ and equation (17) for $\vec{r}'_1$ into equation (15), the expression of distorted lattice vector, $\vec{b}'$ in terms of undistorted vectors is given;

$$\vec{b}' = \vec{b}\,(1 + \psi|\vec{r}|^2) + 2\,\psi\vec{r}(\vec{b}\cdot\vec{r}) + 2\,\theta(\vec{r}\cdot\vec{b})\cdot(\hat{k}\times\hat{r})$$

$$+ \theta\cdot|\vec{r}|^2\,(\hat{k}\times\hat{r}). \qquad (20)$$

At this point t should be recalled that an expression in terms of measurable locations on the plate is sought for the distorted lattice vectors $\vec{a}'$ and $\vec{b}'$. Only the distorted vector $\vec{r}'$ is measured on the plate, not $\vec{r}$ used in equation (20) above.

To find $\vec{r}$ from the measured $\vec{r}'$, equation (14) must be inverted to give $\vec{r}$ as a function of $\vec{r}'$, thus:

$$\vec{r} = f(\vec{r}', \psi, \theta).$$

This inversion follows from the approximation that the two distortions are separate and independent from one another. The effect of spiral distortion is to add a vector to $\vec{r}$ which is in the directon $(\hat{k} \times \hat{r})$, orthogona to $\vec{r}$. The amount by which this added vector changes the magnitude $\vec{r}$ is negligible compared to the effect of the pincushion distortion vector which is in the direction $\vec{r}$. Assuming that the effect of spiral distortion is approximately a rotation of $\vec{r}$ without changing r magnitude, the task of inverting is greatly simplified. First the spiral distortion vector is subtracted from $\vec{r}'$ to give the vector $\vec{r}_\theta'$

$$\vec{r}_\theta' = \vec{r}' - \theta \cdot |\vec{r}'|^3 \, (\hat{k} \times \hat{r}). \tag{21}$$

Using this new vector, the original equation to be inverted takes on the form of a cubic equation,

$$\vec{r}_\theta' = \vec{r} + \psi |\vec{r}|^3 \, \hat{r} \tag{22}$$

equivalently written as,

$$0 = r^3 + n \cdot r + m \tag{23}$$

where

$$n = {}^{1}/_{\psi}$$

$$m = -|\vec{r}'_{\theta}|/\psi$$

There will be one real solution and two imaginary solutions of r if $n^2/4 + m^3/27$ is greater than zero, which is the case since is always positive. The real solution of r is as follows:

$$r = \sqrt[3]{-\frac{m}{2} + \sqrt{\frac{m^2}{4} + \frac{n^3}{27}}} + \sqrt[3]{\frac{m}{2} - \sqrt{\frac{n^2}{4} + \frac{n^3}{27}}} \tag{24}$$

where

$$m = -\left|\frac{\vec{r}'\theta}{\psi}\right|$$

$$= -|\vec{r}' - \theta \cdot |r'|^3 \cdot (\hat{k} \times \hat{r})|/\psi \ .$$

This rather messy equation (24) is the final form of r as a function of ($\vec{r}'$, ψ and θ) and relates the observed $\vec{r}'$ measurements from the plate to the expression of the distorted $\vec{a}'$ and $\vec{b}'$ vectors.

It is important to see that measurements of $\vec{r}'$ on the plate are made relative to an arbitrarily chosen origin, since the true origin of distortion is not known. To go from this arbitrary origin to the distortion origin, a vector $\vec{r}_0$ is added to $\vec{r}'$. The final solution is written in terms of $\vec{r}_0$;

$$m = -|\vec{r}_0 + \vec{r}' - \theta \cdot |\vec{r}'|^3 \cdot (\hat{k} \times \hat{r})| / \psi \qquad (25)$$

where $\vec{r}_0$ is unknown displacement to the true distortion origin.

D. Solution of Least-Squares Function Determines Distortion Origin and Coefficients.

To solve for the 3 unknown parameters $(\psi, \theta, \vec{r}_0)$ in the above equations, a minimization approach is used. The least squares function to be minimized is found by subtracting the right side of the equality in equation (20) from the distorted lattice vectors observed at several different locations in the image. The function is the summed difference of the observed lattice vectors and their theoretical, (calculated) values at different positions, $\vec{r}'_i$, on the image plate,

$$\text{Minimization Function} = \sum_{i=1}^{n} \left((\vec{b}'_{\text{observed}} - \vec{b}'_{\text{calculated}})^2_{r'_i} + (\vec{a}'_{\text{observed}} - \vec{a}'_{\text{calculated}})^2_{r'_i} \right) \qquad (26)$$

Several measurements of $\vec{a}'$ and $\vec{b}'$ at each $\vec{r}'$ position are made from different reciprocal lattice reflections in the diffraction patterns of selected image areas at $\vec{r}'_i$ positions. The minimization function includes measurements of three different reflections as denoted by their h, k values.

$$\text{Min. Function} = \sum_{i=1}^{n}\sum_{i=1}^{m}\left((\vec{b}'_{obs} - \vec{b}'_{calc})^2_{r'_i,\,(h,k)_j} + (\vec{a}'_{obs} - \vec{a}'_{calc})^2_{r'_i,(h,k)_j}\right) \tag{27}$$

where, $\vec{b}'_{calculated}$ is found with equations 20, 24 and 25, and $\vec{a}'_{calc}$ is found by using the identical equations but substituting a' for $\vec{b}'$.

N = total number of diffraction patterns used = 7.

M = total number of diffraction spots used = 3.

The area of the plate covered by the single Gp 32*I crystal specimen is shown in Figure 11. The specimen spanned most of the longer width of the plate and was limited to the upper third region as shown. Assuming that the distortion origin is near the plate center, the specimen is mostly on one side of the distortion origin.

Nine areas of the Gp 32*I protein plate were digitized with the scanning densitometer and their diffraction patterns were obtained using the Fast Fourier transform. A small area, 4 mm square, was

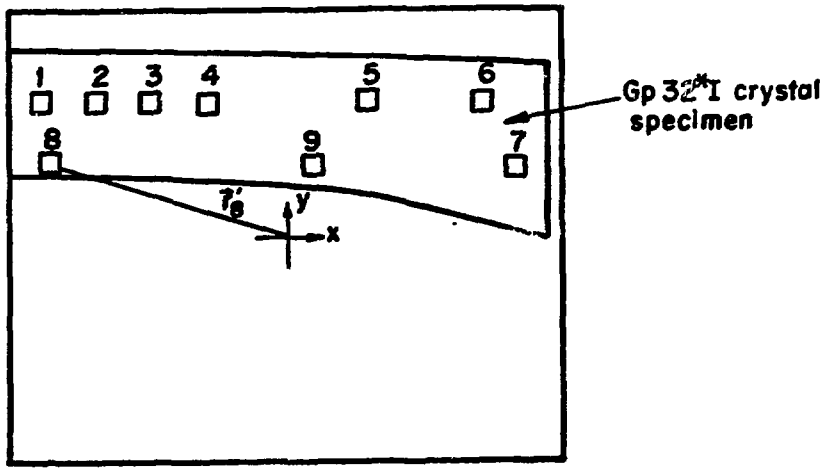

XBL798-3731

Figure 11. A drawing of 4mmx4mm areas scanned on photographic plate. The distorted vector to image area 8, $\vec{r}'_8$, is also shown.

chosen for the scan with the reasoning that local changes in the lattice vectors due to distortions would be minimal over such a small region. The 200 x 200 Fast Fourier Transform was used in exactly the same manner as in the alignment experiments, described in Chapter II.

Three diffraction spots with (h,k) equal to (4,0) (2,$\bar{1}$) and (2,1) were used to measure $\vec{a}'_{obs}$ and $\vec{b}'_{obs}$ vectors. The $\vec{a}$ and $\vec{b}$ undistorted lattice vectors are determined from an area near the center of the plate where the effect of distortions is assumed to be small. The $\vec{a}'$, $\vec{b}'$ vectors are calculated from the row and column position of the reciprocal lattice reflection.

The position of corresponding reciprocal lattice reflections varied from one image to another, and varied by different displacements for different lattice reflections. Table 3 shows the position, in terms of row and column, of each reflection used as data. While some reflections showed no measurable displacement from one image to the next, as much as 2 rows displacement occurred for the (4,0) reflection. These lattice positions were measured by visual examination of the diffraction pattern's power spectrum, in MAGMAP display (Grano). Fractional row and column displacements for lattice reflections split over several array elements were approximated.

The Min. Function, eq. (27) above is minimized on the computer using the very powerful program MINUIT from the CERN Computer Library (13). The upper and lower bounds of all variable parameters are set. The function is minimized by using three different techniques, first by the spline fitting approach and then by gradient

Table 3. Location of scanned image areas.

AREA OF IMAGE	r_x' (μm)	r_y'(μm)
1	-45000	25000
2	-35000	25000
3	-25000	25000
4	-15000	25000
5	15000	25000
6	35000	25000
7	40000	14000
8	-43000	12000
9	5000	12000

Table 4. Location of diffraction spots (row and column coordinates) in 200 by 200 calculated diffraction patterns of 9 scanned image areas, shown in Figure 11.

IMAGE AREA	(H,K)	ROW	COLUMN
1	(2,1)	67.	104.
	(2,1)	91.5	133.
	(4,0)	58.	136.5
2	(2,1)	67.	104.4
	(2,1)	91.	133.
	(4,0)	57.	137.
3		67.	104.
		90.	134.
		55.8	138.
4		66.5	104.
		90.	134.
		55.6	137.
5		67.	104.
		90.	134.
		55.6	137.
6		67.	104.5
		90.3	134.
		55.8	138.
7		67.	104.5
		91.	134.4
		57.	138.
8		67.4	104.
		91.	134.
		57.7	137.
9		66.5	104.
		90.	134.
		55.6	137.

methods. After the function converges to a minimum, the program searchs for other possible minima to guard against convergence to local minima of the function.

The least squares function of distorted lattice vectors converged to a minimum value of 1.0×10^{-9} after being called approximately 1400 times by the CERN minimization program. The cost to run the program was $1.10. The following values of parameters were found:

$\vec{r}_o$ = displacement to distortion origin.

r_{oy} = 18.89 mm

r_{ox} = 10.72 mm

Ψ = 2.6886×10^{-11} μm^{-2}

θ = -8.2475×10^{-12} μm^{-2}

These values of $\vec{r}_o$, Ψ and θ are reasonable since they give a calculate distortion effect which is comparable to measured distortions in the perimeter region of the image. At image position $r_x' = -45000$ μm, $r_y' = 25000$ μm, the calculated magnification change and rotation of diffraction pattern is 4.11 percent and 1.25^o, respectively, which is similar to the observed values of 3.76 percent and 1.13^o.

E. Distortions Correction by Interpolation

Distortion correction reverses the effects of distortions in the image by displacing the image points to their true geometric positions. The mathematical equations which describe the inverse distortion displacements is written here as previously with prime and unprime vectors denoting the distorted and undistorted vectors, respectively.

$$\vec{r}' = x' \hat{i} + y' \hat{j}$$

$$= \vec{r} + \psi \cdot |r|^3 \cdot \hat{r} + \theta \cdot |r|^3 \cdot (\hat{k} \times \hat{r})$$

where

$\vec{r}$ = the vector to the true geometric position of intensity.

$\vec{r}'$ = the vector to position of intensity with pincushion (ψ) and spiral (θ) distortions.

(x',y') = the position of intensity in distorted image.

A regularly spaced array of undistorted image intensities at positions (x,y) is filled by taking intensities from the respective (x',y') positions. In this way an array of intensities representing an undistorted image area is created from the array of distorted image intensities. Rewritting the above equation with an image array vector, $\vec{A}$, in terms

of row and column, and a vector, $\vec{R}$, from distortion origin to area scanned by optical densitometer, gives the following coordinates of the intensities,

$$x' = (Rx + Ax \cdot d) \cdot (1 + (R + A \cdot d)^2) + R^2 \cdot (Ry + Ay \cdot d) .$$

$$y' = (Ry + Ay \cdot d) \cdot (1 + (R + A \cdot d)^2) + \cdot R^2 \cdot (-Rx - A_x \cdot d)$$

$$R = (Rx, Ry)$$

= vector from distortion origins to array element (0,0) of digitized image.

$$\vec{A} = (Ax, Ay) = (\text{column}, \text{row})$$

= array vector from array origin element, (0,0) to position of intensity in terms of rows and columns.

d = unit increment of row and column.

The optical density at coordinates (x',y') is found with an interpolation algorithm. The program first finds the integer row and column position (x',y'), then uses the bilinear interpolation scheme to determine the density at the non-integer array position. The density at (x',y'), determined in this way, is then indexed by its undistorted image position (x,y) and stored in the undistorted array at this integer element index (x,y).

When the bilinear interpolation procedure described above was first used, it sought optical densities at positions outside of the 220 by 220 distorted image array given as data to create a 200 by 200 distortion corrected array. In order to keep the interpolation within bounds of the 220 square array, a constant vector was subtracted from all primed vectors thus bringing the position of intensities within bounds of the array. The array of optical densities produced by the above distortion correction interpolation procedure is Fourier transformed to give a new diffraction pattern. The expected results of diffraction spots being located in the positions of spots of the non distorted image areas from center of the image was not seen. Instead, the diffraction spots were split over several array elements around their array location before the interpolation distortion correction procedure. Therefore the distortion could not have been removed from the image area, and instead, new distortions were apparently introduced by the interpolation.

F. Further Suggestions for Distortion Corrections

Several problems were encountered in the work towards correcting distortions in the image of Gp32* I protein. The following discussion of these problems is written with the goal in mind of future completion of this distortion correction method and to point out the problems which may be inherent to other methods of approach.

The problem of locating the diffraction spots at non integer array positions limited the accuracy of determining the distortion origin and spiral and pincushion distortion coefficients. The position of diffraction spots which are split over two or more array elements was

determined by visual approximation. A better technique of locating the exact position of diffraction spots is needed to improve the data used in the least squares function which finds $\vec{r}_0$, ρ and ψ.

In the distortion correction procedure of section VI.E the problem of interpolating intensities at positions not covered in the 220 by 220 array of image data can be solved by using a larger data array. Ideally, a large image area which covers the central region of the image would be scanned so that the distortion origin is located in one of the data array elements. A limitation of the array size to a maximum size of 256 by 255 resulted from the use of the FTN4 compiler. This limitation may be overcome by using the RUN76 compiler, or possibly with new compilers which will be in use with the CDC7600 computer at LBL in the near future.

Error in determining the distortion origin may result from biased image data due to the specimen covering a limited region of the image. In the image of Gp32* I protein used in all previous experiments, the protein crystal did not cover all quadrants of the image around the distortion origin, as shown in Figure 17. Due to the r^3 dependence of distortions, the distorted lattice vectors are most accurately measured from the perimeter regions of the image. A greater error results in measuring the distortion origin in the lesser width (y-direction) of this image which is covered by specimen only in its upper 1/3 region.

To test the accuracy of all the distortion correction and least squares fit of distortions origin algorithms, a test specimen is ultimately desirable: one which is continuous and covers the entire

area of the image. A computer simulation of image data with a known origin of distortions and distortion coefficients could also be used to test the algorithms. This computer simulated data array can be made by distorting a regular grating or periodic structure with pincushion distortions and spiral distortions using the equation (14) which describe these distortions.

An alternative method to the least squares fitting of the distortion origin and coefficients is to use a deterministic approach in solving for the unknowns in equation (20), (24), and (25). Specimen lattice vectors from three different regions of the image can be used to write three independent equations and the three unknown parameters, $\vec{r}_o$, ψ, and θ may be solved. However, the non-linearity of these equations does not lend itself to an easy solution. Also the use of only three image areas may increase the likelihood of data bias and decreased accuracy in solving for the distortion origin. Such a deterministic approach probably would not prove to be more accurate than the least squares fit of distortion origin used here which has no upper limit to the number of image areas used as data. Also the low cost ($1.10) of running the minimization program to solve for the distortion origin and coefficients allows for a rapid and economic solution.

VII CONCLUSIONS

The methods of rotational and translational alignment of protein patches which used data from computed diffraction patterns were shown to be more successful with respect to cost and accuracy than other methods which used image data. The alignment and addition of four computed diffraction patterns did not result in higher resolution due to the presence of spiral and pincushion distortions in the test specimen image. Although the distortions prevented the coherent addition of diffraction spots in these experiments, they should not be a limiting factor if protein patches are imaged in the central region of the photographic plate where the effect of these assumed projector lens distortions are minimal due to their $\vec{r}$ cubed dependence.

A method of determining the origin of pincushion and spiral distortions in images of crystalline protein has been developed in this paper. The distortion origin and coefficients in the Gp32*I protein image were found by minimizing a least squares function of distorted image lattice vectors. The interpolation algorithm used to correct the image distortions was unsuccessful. A possible problem is that the specimen area covered only a limited region of the image and may have caused bias in the data used to fit the distortion origin. It should be possible to correct the distortions in images, but it will require further testing of all the distortion correction algorithms using simulated data with known distortion origin and coefficients.

ACKNOWLEDGEMENT

I would like to express my appreciation to Dr. Robert M. Glaeser for his help and support in making this work possible. I especially wish to thank Dr. David Grano for the use of several of his computer programs, for his helpful instructions on the use of the LBL computer system, and for several enlightening conversations on image processing. I wish to thank Dr. Wah Chiu, Dr. Steven Hayward and Dr. Owen Saxton for their conversations which have contributed to my education and to this work.

REFERENCES

1. Kuo, I. A. M. and Glaeser, R. M. (1975). "Development of methodology for low exposure, high resolution electron microscopy of biological specimens," Ultramicr 1, 53-66.
2. Glaeser, R. M. (1971). "Limitation to significant information in biological electron microscopy as a result of radiation damage," J. Ultrastruct. 36, 466-482.
3. Unwin, P. N. T. and Henderson, R. (1975). "Molecular structure determination by electron microscopy of unstained crystalline specimens," J. Mol. Biol. 94, 425-440.
4. Unwin, P. N. T. (1975). "Beef liver catalase structure: interpretation of electron micrographs," J. Mol. Biol. 98, 235-242.
5. Chiu, W. and Hosoda, J. (1978). "Crystallization and preliminary electron diffraction study to 3.7Å of DNA helix-destabilizing protein Gp32*I," J. Mol. Biol. 122, 103-107.
6. Glaeser, R. M., Chiu, W. and Grano, D. (1979). "Structure of the surface protein of the outer membrane of Spirillum Serpens," J. Ultrastruc. Res. (in press)
7. Chiu, W., Private communications.
8. Grano, D. A. (1979). "Three-dimensional reconstruction in electron microscopy," Ph.D. Dissertation, University of California, Berkeley.
9. Frank. J. (1973). "Computer processing of electron micrographs," in Advanced Techniques in Biological Electron Microscopy, Ed. J. K. Koehler, (Springer-Verlag, N. Y.), 215-274.

10. Saxton, W. O. and Frank, J. (1977). "Motif detection in quantum noise-limited electron micrographs by cross-correlation," Ultramicr. 2, 219-227.

11. Hillier, J. (1946). "A study of distortion in electron microscopy projection lenses," J. Appl. Phys. 17, 411-419.

12. Liebmann, G. (1952). "Magnetic electron microscopy projector lenses," Proc. Phys. Soc. B65, 94-108.

13. James, F. and Roos, M. (1975) "MINUIT short write-up," in LBL Math and Computing Library.

U.S.GPO:1980-698-169/F-103